

# Multipoint correlations of concentration fluctuations in a turbulent passive scalar field

R. J. Miller · P. Dasi · D. R. Webster

Received: 18 January 2007 / Revised: 18 October 2007 / Accepted: 6 November 2007 / Published online: 28 November 2007  
Springer-Verlag 2007

**Abstract** This study experimentally analyzes a turbulent passive scalar field (Shraiman and Siggia 1990). In general, the correlation function associated with the concentration fluctuations of the concentration fluctuations. The instantaneous measurement points is:  $C_N = \langle \theta(r_A, t) \theta(r_B, t) \dots \theta(r_N, t) \rangle = \langle \theta_A \theta_B \dots \theta_N \rangle$  (1) where  $r_A, r_B, \dots, r_N$  denote the spatial location of the measurement points,  $\theta$  is the instantaneous concentration fluctuation at the specified measurement point, and  $\langle \dots \rangle$  indicates time-averaging. Analyzing turbulent scalar fields by evaluating multipoint correlators deviates from traditional efforts, which focused on measurements at one or two points in space or the visual identification of scalar structure. Although two-point correlations provide some insight to the scalar field (see Tavoularis and Corrsin 1981), the presence of ramp-cliff structures and small-scale anisotropy requires the analysis of multipoint statistics (Warhaft 2000). Ramp-cliff structures are ubiquitous in turbulent scalar fields and have been observed in shear flows (e.g. Mestayer et al. 1976; Sreenivasan et al. 1979), grid turbulence (e.g. Tong and Warhaft 1994), and numerical simulations (e.g. Pumir 1994; Holzer and Siggia 1994; Celani et al. 2000; Schumacher and Sreenivasan 2003). An advantage of multipoint correlators is that the spatial orientation of scalar filaments can be analyzed while the scaling exponent properties are retained. Therefore, multipoint correlators naturally extend traditional research methods and provide a framework to probe the scalar field for the spatial orientation of the scalar filaments. The current study experimentally focuses on analyzing three-point correlation functions of concentration fluctuations in a turbulent shear flow.

In pursuit of symmetry and scaling properties of multipoint correlations, Shraiman and Siggia (1995, 1996, 1998), Pumir (1998), and Celani and Vergassola (2001) theoretically and numerically explored idealized turbulent

Abstract This study experimentally analyzes a turbulent passive scalar field (Shraiman and Siggia 1990). In general, the correlation function associated with the concentration fluctuations of the concentration fluctuations. The instantaneous measurement points is:  $C_N = \langle \theta(r_A, t) \theta(r_B, t) \dots \theta(r_N, t) \rangle = \langle \theta_A \theta_B \dots \theta_N \rangle$  (1) where  $r_A, r_B, \dots, r_N$  denote the spatial location of the measurement points,  $\theta$  is the instantaneous concentration fluctuation at the specified measurement point, and  $\langle \dots \rangle$  indicates time-averaging. Analyzing turbulent scalar fields by evaluating multipoint correlators deviates from traditional efforts, which focused on measurements at one or two points in space or the visual identification of scalar structure. Although two-point correlations provide some insight to the scalar field (see Tavoularis and Corrsin 1981), the presence of ramp-cliff structures and small-scale anisotropy requires the analysis of multipoint statistics (Warhaft 2000). Ramp-cliff structures are ubiquitous in turbulent scalar fields and have been observed in shear flows (e.g. Mestayer et al. 1976; Sreenivasan et al. 1979), grid turbulence (e.g. Tong and Warhaft 1994), and numerical simulations (e.g. Pumir 1994; Holzer and Siggia 1994; Celani et al. 2000; Schumacher and Sreenivasan 2003). An advantage of multipoint correlators is that the spatial orientation of scalar filaments can be analyzed while the scaling exponent properties are retained. Therefore, multipoint correlators naturally extend traditional research methods and provide a framework to probe the scalar field for the spatial orientation of the scalar filaments. The current study experimentally focuses on analyzing three-point correlation functions of concentration fluctuations in a turbulent shear flow.

## 1 Introduction

Multipoint correlations of scalar fluctuations provide a tool to evaluate the symmetry and scaling behavior of turbulent

R. J. Miller · L. P. Dasi · D. R. Webster (✉)  
School of Civil and Environmental Engineering,  
Georgia Institute of Technology, Atlanta, GA 30332-0355, USA  
e-mail: dwebster@ce.gatech.edu

flow fields. Shraiman and Siggia (1995) employed the Hopf equation to derive the three-point correlation function. In the inertial-convective subrange, each solution can be fully described using scaling exponents (Shraiman and Siggia 1996, 2000; Mydlarski et al. 1998). The general conclusion of these studies is that anomalous scaling of the scalar fluctuations is seemingly universal and indicates the persistence of small-scale anisotropy.

Experimental efforts to verify the theoretical predictions have been limited to the three-point correlation measurements of a nearly homogeneous and isotropic turbulent flow field (Mydlarski and Warhaft 1998; Mydlarski et al. 1998). The sampling configuration employed two cold wire probes arranged with transverse spacing. Taylor's frozen

flow hypothesis was employed to transform one-dimensional time records to a spatial displacement in the flow direction, hence defining three points for evaluation of the three-point correlation function. The resulting coordinate system is depicted in Fig. 1. The modified coordinate system shown in Fig. 1b was introduced because Mydlarski and Warhaft (1998) observed symmetry about the line  $x_2 = 2x_1$ . Mydlarski and Warhaft (1998) concluded that the observed uniform flow depth of  $H = 100$  mm. The flume head box symmetry is a result of the presence of ramp-cliff structures. Since ramp-cliff structures appear in shear flows as well as non-shear flows, they speculate that the symmetry with low turbulence intensity. Measurements of the passive scalar field were obtained 23 m from the channel inlet to ensure the turbulent boundary layer was fully developed. A coordinate system was defined such that  $x_1$  was the streamwise direction,  $x_2$  was the bed-normal direction, and  $z$  was the transverse direction spanning the channel. The origin of all coordinates was defined at the point source of the scalar field (described further below). Since the flow was fully developed in the  $x_1$ -direction and transversely uniform in the  $x_2$ -direction, the velocity field was inhomogeneous only in the bed-normal direction. As shown in Fig. 2, the measured mean velocity profiles agree very well with the law-of-the-wall profile ( $\kappa = 0.41$  and  $C = 5.5$ ). The Reynolds stress profiles (shown in Dasi et al. 2007) also agree with previous measurements of Tachie et al. (2003) and DNS results of Spalart (1988) for similar  $Re_\theta$ . The flow characteristics are summarized in Table 1.

The purpose of this study is to employ multipoint correlation functions to examine the small-scale behavior of a high Schmidt number passive scalar field in a turbulent boundary layer (shear flow). To date, Mydlarski and Warhaft (1998) reported the only experimental data (low Schmidt number, non-shear flow) for multipoint correlation functions to complement the theoretical and numerical efforts of Shraiman and Siggia (2000) and others. The current research provides an experimental examination

of the effect of the initial injection length scale and Reynolds number. As a first step, two-point correlations of the fluctuating scalar field are analyzed to estimate the integral length scale and compare to previous results. The three-point correlation functions of the fluctuating scalar field are examined to determine the scaling exponent properties, extract geometric relationships of the scalar elements, and evaluate the small-scale structure of the concentration field.

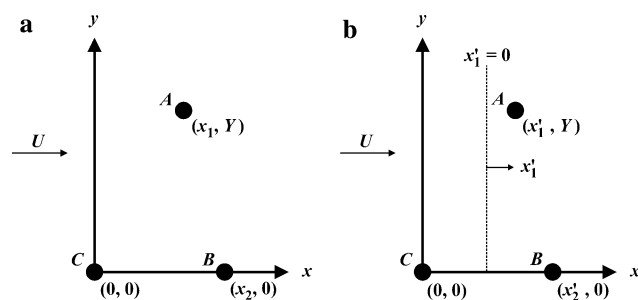


Fig. 1 Coordinate system employed by Mydlarski and Warhaft (1998) for the analysis of the three-point correlation of the scalar fluctuations: a coordinate system, and b modified coordinate system defined by  $(x'_1, x'_2) = (x_1 - 0.5x_2, x_2)$

The turbulent passive scalar field was developed through the iso-kinetic release of a high Schmidt number dye (Rhodamine 6G,  $Sc = \nu/\Gamma \approx 1,250$ ,  $\nu = 1 \times 10^{-6}$  m<sup>2</sup>/s, and  $\Gamma \approx 8 \times 10^{-10}$  m<sup>2</sup>/s) into the inertial layer of the turbulent boundary layer. The center of the release nozzle was located 50 mm above the bed surface (160, 320, and 530, respectively for the three cases) along the flume centerline. Three nozzle diameters ( $D/H = 0.022$ , 0.047, and 0.094, respectively) were employed. In each case, a streamlined fairing was attached to the release nozzle to minimize the

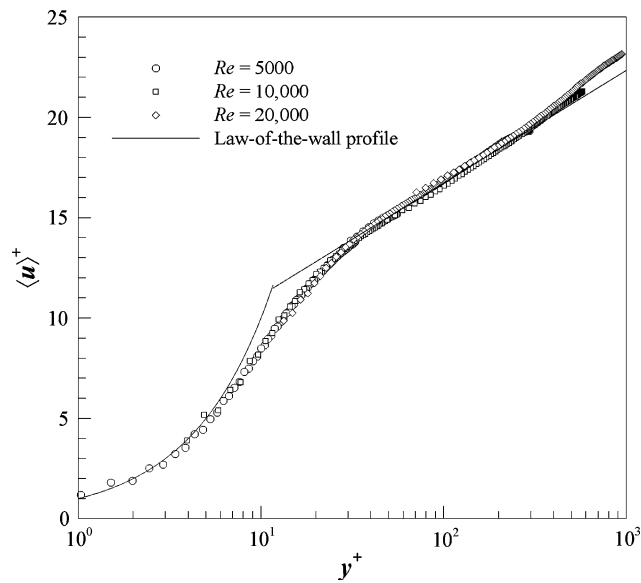


Fig. 2 Normalized mean velocity profiles. Data adapted from Dasgupta et al. (2007)

wake perturbation. The iso-kinetic release and streamlined fairing minimized the shear flow generated by the scalar release nozzle. Therefore, the subsequent mixing process was a result of the fully developed turbulent boundary layer flow. We generally expect that the properties of the scalar field will be influenced by the nozzle diameter, especially in the vicinity of the release location. An example flow visualization image is shown in Fig. 3.

The current study analyzes two cases of the collected data. The first case considers the effects of the injection length scale in the presence of a constant Reynolds number (i.e.  $Re = 10,000$ ;  $D = 2.2, 4.7, \text{ and } 9.4 \text{ mm}$ ). The second case analyzes the effects of different velocity fields in the presence of a constant injection length scale

Table 1 Summary of the flow characteristics

$Re$	$D$ (mm)	$u^*$ (mm/s)	$\eta$ ( $\mu\text{m}$ )	$\eta_B$ ( $\mu\text{m}$ )	$\frac{d\langle U \rangle}{dy}$ (1/s)	$u'$ (mm/s)	$Re_\lambda$	$D/\eta$
5,000	4.7	3.25	760	24	0.18	5.3	60	6.2
10,000	2.2							5.2
10,000	4.7	6.4	420	13	0.38	11.8	90	11.1
10,000	9.4							22.4
20,000	4.7	10.6	290	9	0.70	19.1	120	16.2

The Kolmogorov microscale was estimated as  $\eta_K \approx \left(\frac{\nu^3}{\epsilon}\right)^{1/4}$ , and the Batchelor scale was estimated as  $\eta_B \approx \left(\frac{\nu \Gamma^2}{\epsilon}\right)^{1/4}$ . The turbulent kinetic energy dissipation rate was based on scaling estimates of the turbulence intensity and integral length scale  $\frac{\langle U \rangle}{y}$  and  $u'$  are the mean velocity gradient and velocity rms, respectively, at the nozzle elevation



Fig. 3 Dye visualization image for  $Re = 10,000$  and  $D = 4.7 \text{ mm}$ . The flow direction is left to right

(i.e.  $D = 4.7 \text{ mm}$ ;  $Re = 5,000, 10,000, \text{ and } 20,000$ ). The fluctuating scalar field associated with each case was measured at six distances downstream from the release location:  $x = H, 2.5H, 5H, 10H, 20H, \text{ and } 40H$ .

The concentration field was quantified with the planar laser-induced fluorescence (PLIF) technique. The fluorescent tracer (Rhodamine 6G) was released iso-kinetically to create a plume as described above. An Argon-ion laser beam (514 nm, Coherent Innova 90) was focused at the measurement location (50 mm above the flume bed) using a 6 $\times$  beam expander and a 2 m focal length symmetrical convex lens. The beam diameter/waist diameter was measured as approximately 80  $\mu\text{m}$ , and the Rayleigh length corresponding to this configuration was calculated as 20 mm. The laser sheet was formed by sweeping the laser beam through the measurement region ( $x-y$  plane) using scanning mirrors. The scanning system consisted of a mirror mounted on a galvanometer (Cambridge Technology) positioned above the water surface. A National Instruments multifunction input/output board generated the voltage signal that controlled the mirror position. The scan time of 3 ms ensured sufficient illumination of the tracer field while limiting the horizontal distortion of the dye filaments due to advection to less than 3% for the fastest flow ( $Re = 20,000$ ). The distortion was less for the slower flow cases with a maximum of 1.5 and 0.75% for  $Re = 10,000$  and 5,000, respectively.

The emitted light was collected with a 12-bit CCD camera with  $1392 \times 1024$  pixels (LaVision). A long-pass optical filter (Tiffen Orange 21) was used to eliminate scattered laser light from the images. A Nikon MicroNikkor macro lens (200 mm) provided an image resolution of approximately 13  $\mu\text{m}/\text{pixel}$ . The image resolution was comparable to the Batchelor length scale (Table 1) whereas the laser sheet thickness was larger. 12,000 instantaneous images were captured at each of the six downstream distances for each plume at a rate of 10 frames per s.

To calibrate the PLIF measurement system, the measurement area was sequentially flooded with uniform solutions of at least eight prescribed concentrations ranging from 0 to 100  $\mu\text{g}/\text{L}$  of Rhodamine 6G. The average pixel intensity was calculated based on a series of 200 images captured for each uniform solution. The calibration images were corrected for laser attenuation due to the presence of Rhodamine 6G (Ferrier et al. 1993). For each pixel in the

camera array, a linear regression analysis was employed to derive the relationship between the dye concentration and the corrected pixel intensity. These calibration functions were subsequently used to convert the raw images of the plume structure to concentration field data.

Measurement uncertainty came from errors in determining the concentration of the calibration fluid and the errors due to digitization in the camera. The error in the calibration fluid concentration was estimated to be less than  $\pm 2.5\%$ . The worst case digitization error was for the lower end of the pixel intensity range and was estimated to be  $\pm 3\%$  for the collected data. Combining these estimates, the overall bound for the individual concentration measurements was less than  $\pm 4\%$ .

Two- and three-point correlation functions were calculated by direct evaluation of Eq. 4 using the PLIF concentration fields. To increase the number of sample the correlation function was calculated for many pixel locations within a small spatial region for each instantaneous concentration field. The spatial region corresponds to a  $512 \times 512$  pixel ( $6.6 \times 6.6$  mm) region near the center of the image (shown in Fig. 4). This region was defined because the mean concentration gradient ( $d\langle\Theta\rangle/dy$ ) was nearly constant within these 3 boundaries. The uniform mean concentration gradient region was preferred to ensure that large-scale characteristics of the concentration field were uniform throughout the region. Figure 5 shows the mean concentration profiles for the  $Re = 10,000$  and  $D = 4.7$  mm case, which demonstrates the nearly constant mean concentration gradient in the defined sub-region. Figure 6 also shows that the mean concentration gradient decreases with distance from the source as the concentration field becomes more dilute and homogeneous due to turbulent mixing. The mean flow advected individual filaments beyond the limits of the measurement region between consecutive images, and the advected length was also large compared to the integral length scale. Hence, the structure in each field was unique from the previous field and the samples were statistically independent. The calculation procedure increased the number of samples (of the correlation function) to several million; the exact number was dependent on the multipoint configuration. For instance, 500 evaluations of the correlation function in each instantaneous field yielded 6 million total samples, which was the smallest number of samples of the reported data. We calculated the standard error of the correlation calculation as a function of the number of samples. In each case, the standard error converged to a constant value for the number of samples included. The results indicate that for 6 million samples, the standard error of the average correlation function was less than 4%.

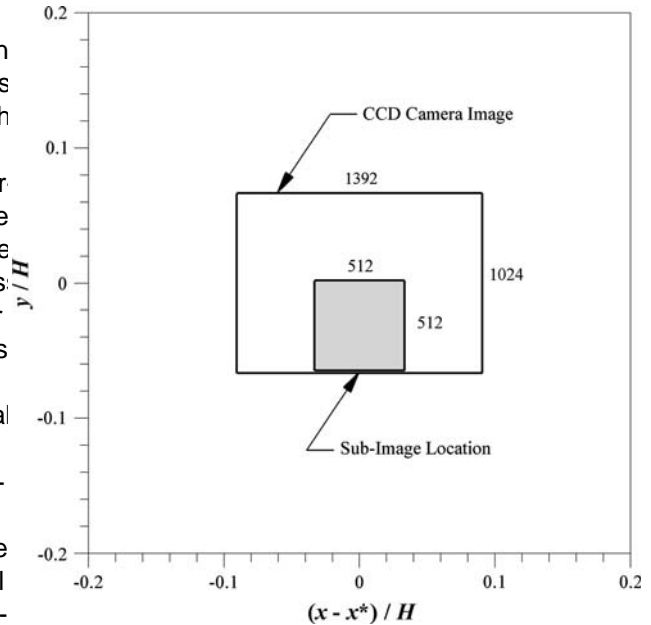


Fig. 4 The measurement region (shaded area) associated with  $x^* = 0.1, 0.25, 0.5, 1.0, 2.0,$  and  $4.0$  m. In the measurement region, the mean concentration gradient is nearly constant at  $x^* = 0.1, 0.25, 0.5, 1.0, 2.0,$  and  $4.0$  m.

Characteristics of the fluctuating concentration field are apparent in Fig. 3, the scalar field possesses large-scale intermittency. Figure 6 shows profiles of the intermittency factor along the centerline of the plume. Chatwin and Sullivan (1989) define the intermittency factor as the fraction of time that the scalar concentration is greater than a threshold value. In Fig. 6, the threshold value is equal to

Characteristics of the fluctuating concentration field are apparent in Fig. 3, the scalar field possesses large-scale intermittency. Figure 6 shows profiles of the intermittency factor along the centerline of the plume. Chatwin and Sullivan (1989) define the intermittency factor as the fraction of time that the scalar concentration is greater than a threshold value. In Fig. 6, the threshold value is equal to

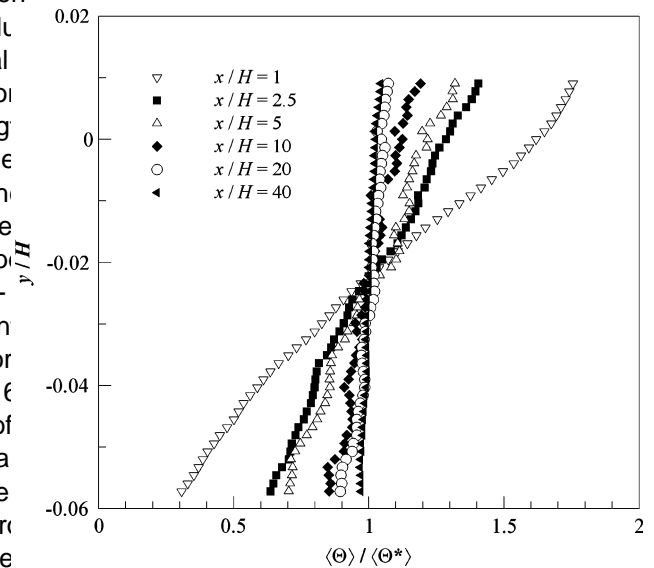


Fig. 5 Concentration profiles for  $Re = 10,000$  and  $D = 4.7$  mm.  $\langle\Theta^*\rangle$  is the local spatially averaged value, which centers the normalized profiles around unity for comparison

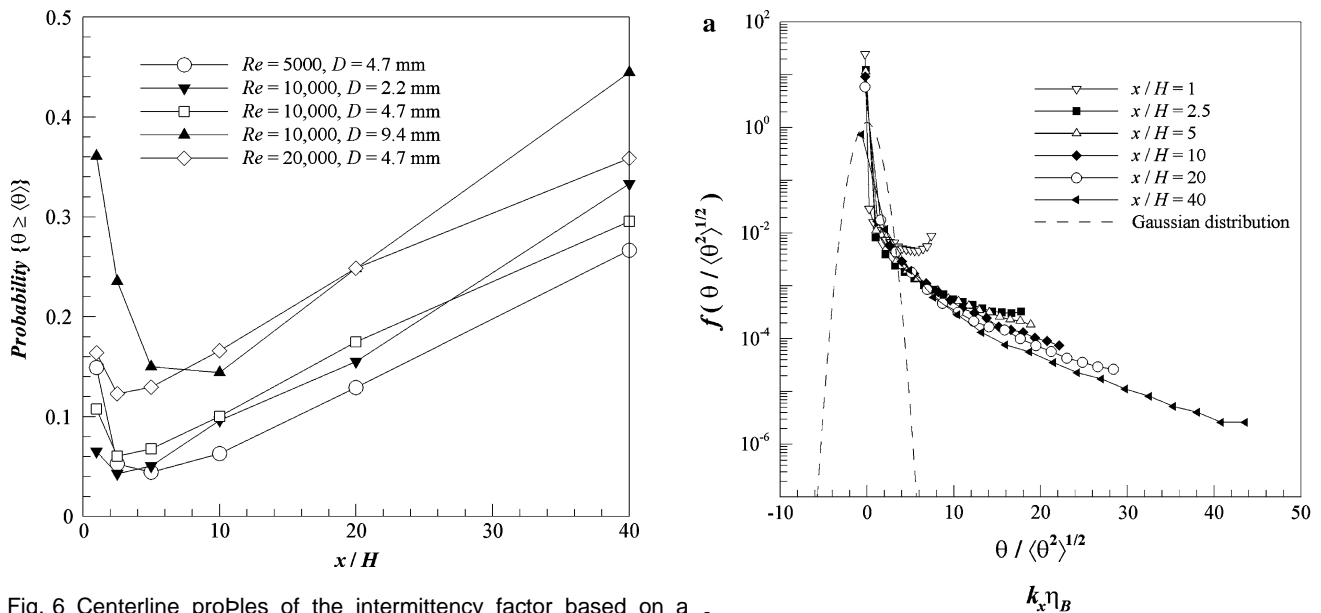


Fig. 6 Centerline profiles of the intermittency factor based on a threshold equal to the local time-averaged concentration

the mean concentration. The figure shows an initial decrease of intermittency factor (from the initial value of 1.0) reaching a minimum value followed by a gradual increase toward the value of 0.5 (corresponding to a Gaussian distribution). In general, the intermittency factor in this range increases with both Reynolds number and injection length scale. Therefore, concentrated dye filaments are encountered more frequently at a point in the field with increasing Reynolds number or increasing injection length scale.

As a preliminary description of the fluctuating concentration field, Fig. 7 shows PDFs of the scalar fluctuations normalized by the standard deviation and the one-dimensional longitudinal power spectra of the passive scalar field at six distances from the source nozzle. Here, we present data for  $Re = 10,000$  and  $D = 4.7$  mm, and the other cases are available in Das [2004](#). Figure 7a shows the evolution of the PDF from bi-modal near the source nozzle to that with an elongated tail. Fluctuations greater than 40 standard deviations were observed. The length of the tail of the PDF appears to grow with increasing distance from the source. Also, the PDF distributions appear to collapse on the same normalized trend with increasing distance from the source. Although the PDFs of the scalar derivatives are not shown here, their skewness of the scalar derivative in both the longitudinal and vertical directions was on the order of one for this scalar field.

In Fig. 7b, each power spectrum shows evidence of scaling behavior in the inertial-convective range. The slope of the spectrum in the inertial-convective range roughly matches the traditional  $k_x^{-5/3}$  profile except for the spectrum located closest to the source ( $x/H = 1$ ), which decreases more rapidly in this regime and appears to be influenced by the source nozzle dimension. There is a transition around

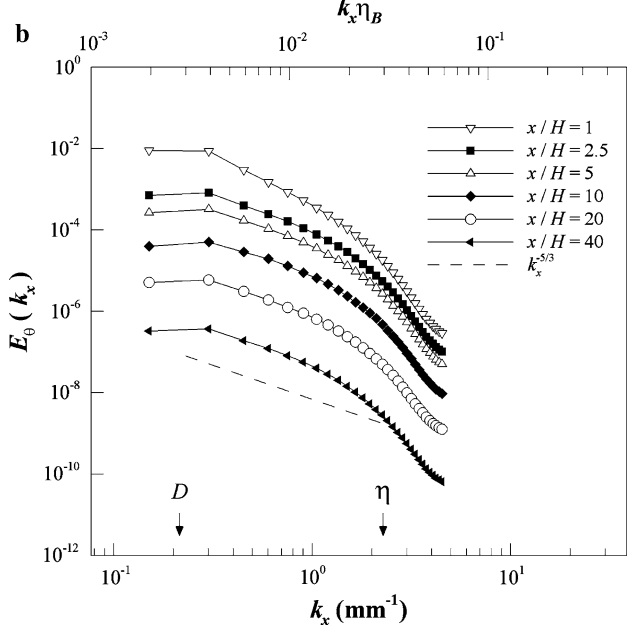


Fig. 7 a Probability density functions of the scalar fluctuations normalized by the standard deviation, and longitudinal spectra of the fluctuating scalar field for  $Re = 10,000$  and  $D = 4.7$  mm

the wave-number corresponding to the Kolmogorov length scale with greater magnitude of the spectral slope appearing in the viscous-convective regime. The spectral profiles appear nearly parallel in the viscous-convective regime without significant variation with distance from the source.

Two-point correlation of the concentration fluctuations

The two-point correlation function of the fluctuating scalar field was calculated for the plane defined by the streamwise

and wall-normal directions (i.e. the  $x - y$  plane). In an isotropic scalar field, the two-point correlation contours in the  $x - y$  plane would be symmetric, concentric circles. Tavoularis and Corrsin (1981) reported that the contours develop a tilted, asymmetric, elliptical shape as a result of the mean velocity shear. The tilted orientation of the two-point correlation function results from the mean velocity shear tilting and stretching the scalar elements into a preferential orientation.

The two-point correlation contours in the current study also exhibit the characteristic elliptical shape that develops as the mean velocity shear acts on the scalar field. Figure 8 illustrates the transformation of the two-point correlation contours as the scalar field evolves downstream. In Fig. 8a,  $r_i$  denotes the spatial separation vector of the two points (where  $i$  takes the value of 1 or 2 to represent the streamwise  $x$  or wall-normal  $y$  directions, respectively). The untilted, elliptical shape observed for the contours in Fig. 8a appears to be a result of the tracer injection method. The iso-kinetic release of the tracer preferentially aligns the scalar elements with the streamwise direction. As a result, the major axis of the elliptical contour shape is aligned with the streamwise direction.

Figure 8b shows that as the plume evolves downstream and the mean velocity gradient acts on the scalar field, the two-point correlation contours develop a tilted, elliptical shape. As the scalar field is advected downstream, the effects of the tracer injection method diminish at these length scales and the alignment of the two-point correlation contour is dictated by the mean velocity shear. The mean velocity shear preferentially tilts the element structure, and the characteristic oval shape of the correlation contour correspondingly tilts. This behavior was observed for each injection length scale and each Reynolds number and is consistent with the data reported by Tavoularis and Corrsin (1981).

## 5 Integral length scale of the scalar field

The integral length scale  $l_L$  describes the separation distance beyond which the correlation of the concentration fluctuations is poor:

$$l_L = \int_0^{\infty} \frac{C_2(r)}{\langle \theta_A^2 \rangle} dr \quad (2)$$

where  $C_2 = \langle \theta_A \theta_B \rangle$  is the two-point correlation function and  $r$  is the distance between the two points. Physically, the integral length scale is related to the size of the elements. At intermediate downstream distances ( $2.5/H < 10$ ), the integral length scale associated with the streamwise and wall-normal directions approach equivalent values. At these intermediate downstream distances, the integral

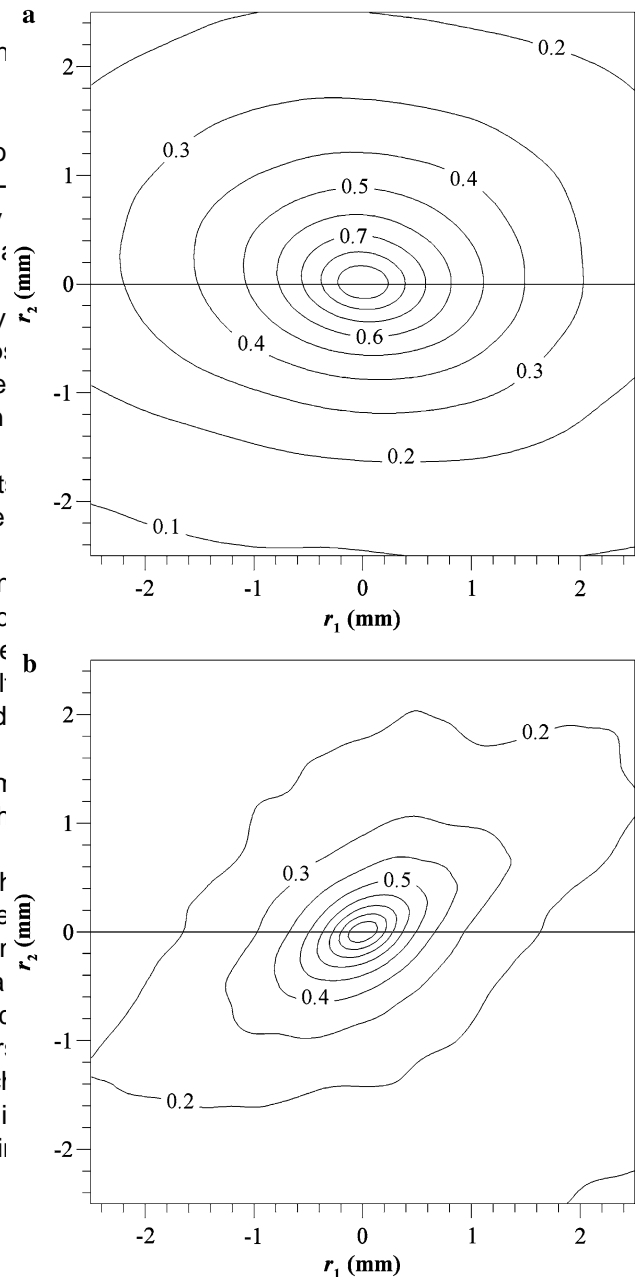


Fig. 8 Contours of the two-point correlation function of the fluctuating scalar field ( $C_2/\langle \theta_A^2 \rangle$ ) for  $Re = 10,000$  and  $D = 4.7$  mm at a  $x/H = 1$ , and b  $x/H = 40$

and wall-normal directions. Close to the release location ( $H = 1$ ), the integral length scale in the streamwise direction is greater than the integral length scale in the wall-normal direction (Fig. 9a). Again, the difference arises from the preferential alignment with the streamwise direction of the elements near the release location (see Fig. 8a). At intermediate downstream distances ( $2.5/H < 10$ ), the integral length scale associated with the streamwise and wall-normal directions approach equivalent values. At these intermediate downstream distances, the integral

length scale is weakly dependent on the Reynolds number but appears to strongly depend on the injection length scale. This intermediate phase may be interpreted as the region where an initially well aligned scalar field has been mixed by a few eddy turnovers resulting in a distribution of filaments with random orientation. Therefore, the integral length scales in both directions approach the same value (i.e. the points closest to the dashed line in Fig. 9). As the scalar field evolves further ( $x/H > 20$ ), the integral length scale associated with each direction remains roughly constant or increases slightly as the influence of the mean velocity shear becomes more dominant. When the integral length scale is scaled by the injection length scale (i.e. the release nozzle diameter), the normalized integral length scale is smallest for the larger injection size ( $D = 9.4$  mm) and largest for the smaller injection size ( $D = 2.2$  mm) for all distances from the release location (Fig. 9b). Hence, the larger injection length scale yields relatively smaller filaments in the plume. This trend results from the relative size of the turbulent eddies compared to the initial filament size. As the source nozzle size increases, the range of turbulent eddies stirring the filament increases (for the same  $Re$ ), thus generating relatively finer scalar structure. The integral length scale is used in subsequent three-point correlation calculations to specify the spacing of the sample points.

### 6 Three-point correlations of the concentration fluctuations

The advantage of the current measurement approach is that the planar concentration data allows for direct examination of many geometric arrangements of the three points defined for the correlation function calculation. Specifically, the size, shape, and orientation of the triangle formed by the three points can be varied over a large parameter space. Nevertheless, as a first step in the evaluation of the three-point correlation functions, the point configuration of Mydlarski and Warhaft (1998) is employed. Examining the Mydlarski and Warhaft (1998) configuration facilitates a comparison to the previous experimental data and an extension of their observations to shear flows.

#### 6.1 Configuration of Mydlarski and Warhaft (1998)

As discussed in the Introduction, Mydlarski and Warhaft (1998) analyzed three-point correlations of the fluctuating scalar field for a nearly homogeneous and isotropic flow. The point configuration was developed using two cold wire probes and Taylor's frozen turbulence hypothesis. Figure 1 illustrates the three-point geometry, which

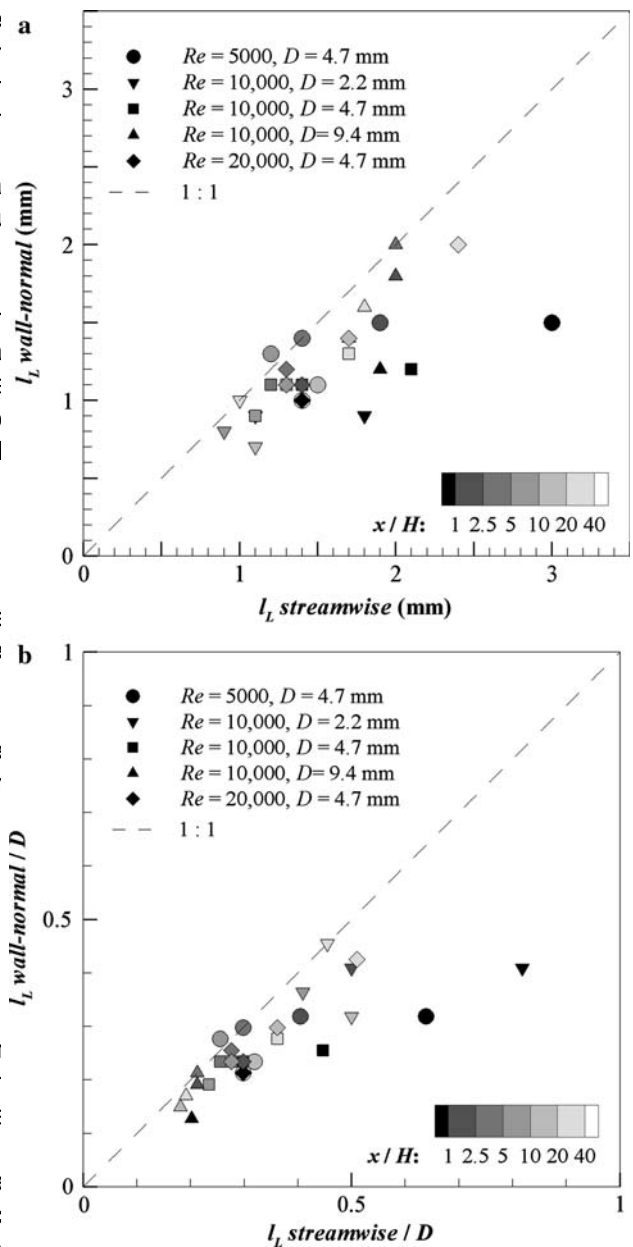


Fig. 9 Integral length scale of the scalar field in the streamwise and wall-normal directions. a Dimensional, and b normalized by the release nozzle diameter

consists of reference point C, point B displaced in the streamwise direction a distance  $\delta_x$ , and point A displaced in the streamwise direction a distance  $\delta_x$  and in the wall-normal direction a distance  $\delta_y$ . For the current evaluation of the planar concentration data, the Taylor frozen turbulence hypothesis is not needed. The appropriate wall-normal separation distance  $\delta_y$  was specified based on the integral length scale such that  $\delta_x/l_L \cong 0.05$ . This value is comparable to that employed by Mydlarski and Warhaft (1998) who reported data for  $\delta_x/l_L \cong 0.043, 0.051, \text{ and } 0.13$ .

Figure 10 show contours of the correlation function in the modified coordinate system  $x'_1$  and  $x'_2$  for three distances from the release location. The three-point correlation,  $\langle \theta_A \theta_B \theta_C \rangle$ , is normalized by the negative correlation evaluated at  $x'_1 = x'_2 = 0$  (i.e. the representation  $-\langle \theta_A \theta_B \theta_C \rangle / \langle \theta_A \theta_C^2 \rangle = -C_3 / \langle \theta_A \theta_C^2 \rangle$ ). In all cases, the innermost contours are nearly symmetric, concentric, circular shapes. The size of the innermost contours constricts slightly with increasing  $Re$ , which suggests that smaller separation distances are required to maintain a significant correlation between the three points. The outermost contours appear close to symmetric about both  $x'_1 = 0$  and  $x'_2 = 0$ ; however, the shape varies depending on the flow conditions. Note the hexagonal shape associated with the outermost contours in Fig. 10a at  $x/H = 1$  and the V-shape that the outermost contours exhibit in Fig. 10d at  $x/H = 1$ .  $\hat{O}\hat{O}$ -shape refers to the shape of the contours for  $x'_2 > 0$  centered around  $x'_1 = 0$  (a similar contour shape is observed in inverted form for  $x'_2 < 0$ ). Most of the contour fields exhibit a basic hexagonal shape for the outer contours. The shape of the hexagonal contour is slightly concave in many cases shown in Fig. 10, which suggests that the contour pattern is tending toward the  $\hat{O}\hat{O}$ -shape that is most clearly observed in Fig. 10d at  $x/H = 1$ .

Figure 10 also demonstrates the behavior of the three-point correlation contours as the scalar field evolves downstream. In all cases, the innermost contours constrict and the symmetric, concentric, circular shape remains as the mean velocity shear acts on the scalar field. The outermost contours become distorted, but the symmetry remains basically intact (both about  $x'_1 = 0$  and  $x'_2 = 0$ ). The contours that demonstrate the poorest symmetry corresponds to the  $Re = 10,000, D = 2.2$  mm case at  $x/H = 40$  (Fig. 10b). For the  $Re = 10,000, D = 9.4$  mm case (Fig. 10d), the V-shape pattern of the outer contours evolves toward the hexagonal pattern with increasing distance from the release location.

The results of the current study indicate that the V-shape contour pattern emerges but does not exhibit all the properties reported by Mydlarski and Warhaft (1998). Possible reasons for the differences include asymmetry in the wall-normal direction and skewness of the scalar signal. The mean velocity shear in the current study leads to asymmetry in the wall-normal direction. Thus, if the scalar gradient is flipped, the third-order statistics will change due to the mean velocity gradient. In contrast, Mydlarski and Warhaft (1998) reported that odd symmetry in the y-direction existed in their data. In addition, they reported that the correlation function should be zero when the three points form an equilateral triangle. This condition is a consequence of the imposed symmetry required to derive the three-point correlation function based on the structure function. Mydlarski and Warhaft (1998) calculated the

structure function as a surrogate for the correlation function because of concerns regarding measurement drift between the cold wire probes. Due to the direct evaluation of the correlation function and lack of symmetry in the current data, the correlation function was not zero for the equilateral triangle configuration. In addition, as part of the derivation relating the structure function to the correlation function, Mydlarski and Warhaft (1998) assumed the scalar (signal) skewness was zero, which was consistent with their data. As suggested in Fig. 10, the scalar (signal) skewness is non-zero and is as large as 40 in some cases for the current data. The asymmetry of the concentration fluctuations is further demonstrated by the intermittency factor shown in Fig. 6.

## 6.2 Configuration based on the shape function

As mentioned above, the current data facilitate evaluation of arbitrary three point configurations in the measured plane, without relying on assumptions such as the validity of the Taylor frozen turbulence hypothesis. The three-point correlation of the fluctuating scalar field depends on the location of unique points in space because of the relative orientation of the filament structure. As a result, the correlation function is dependent on the size, shape, and orientation of the triangle formed by the three points. Celani and Vergassola (2001) reported that the three-point correlation function can be formulated as:

$$C_3 = \langle \theta_A \theta_B \theta_C \rangle = R^{\zeta_3} f(\chi, w) \cos \phi + \text{Subdominant higher order terms} \quad (3)$$

where  $f(\chi, w)$  describes the effects of different triangular shapes,  $\phi$  describes the orientation of the triangle with respect to the mean scalar gradient, and the scaling exponent of the global size variable  $R$ , (a characteristic length scale of the triangle formed by the three points):

$$R = \sqrt{\frac{r_{AB}^2 + r_{BC}^2 + r_{CA}^2}{3}} \quad (4)$$

where  $r_{ij}$  is the distance between the points  $i$  and  $j$ . The parameters associated with the shape factor and  $\vec{p}_1, \vec{p}_2$  are defined using the Euler parameterization described by Shraiman and Siggia (1998) and Pumir (1998). Using the following definitions:

$$\vec{p}_1 = \frac{\vec{r}_1 - \vec{r}_2}{\sqrt{2}} \quad \text{and} \quad \vec{p}_2 = \frac{\vec{r}_1 + \vec{r}_2 - 2\vec{r}_3}{\sqrt{6}} \quad (5)$$

where the spatial locations of points  $A, B$ , and  $C$  are denoted as  $\vec{r}_1, \vec{r}_2$ , and  $\vec{r}_3$ , respectively, the parameters associated with the shape factor are:

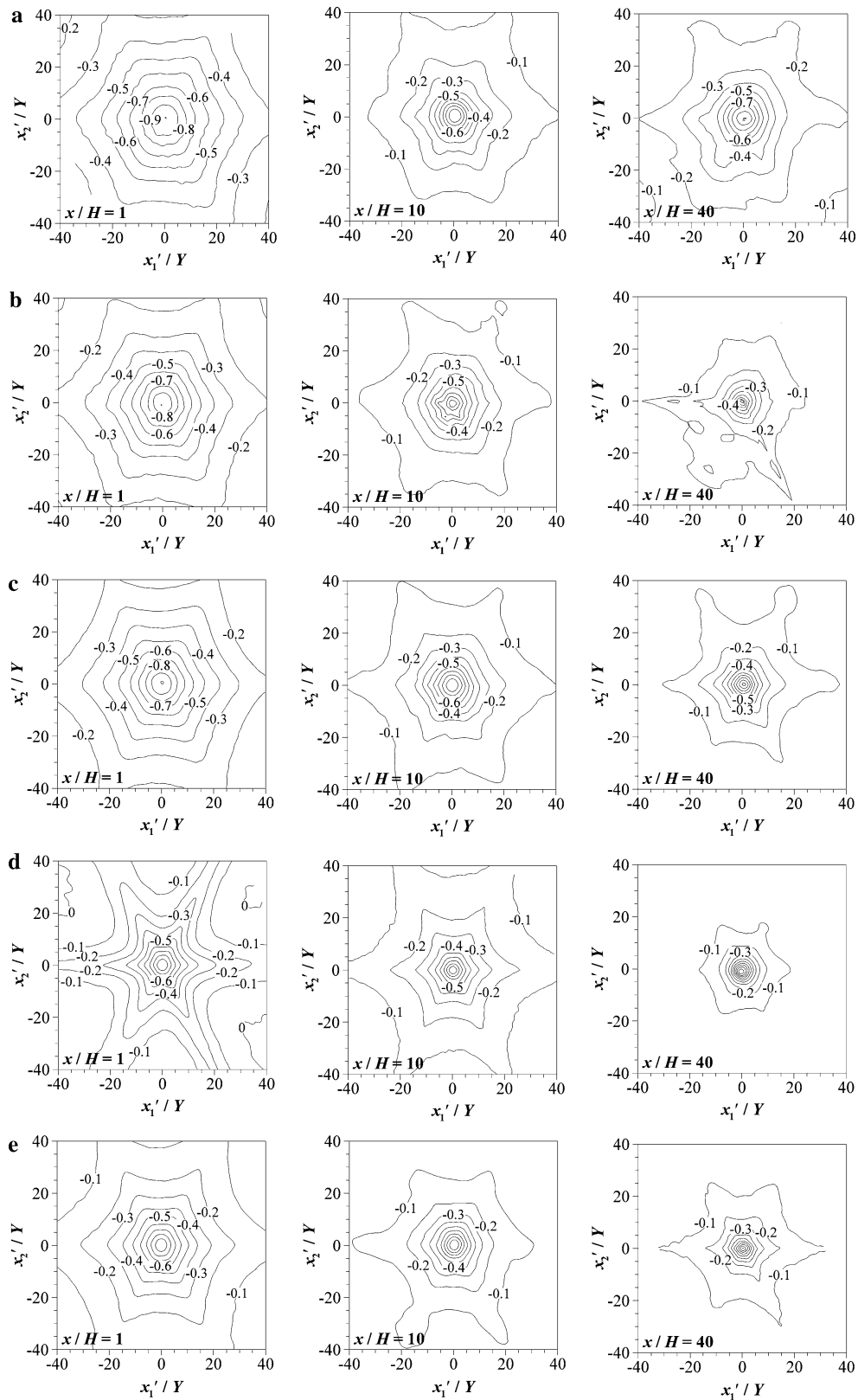


Fig. 10 Contours of the three-point correlation function of the and  $D = 2.2$  mm,  $cRe = 10,000$  and  $D = 4.7$  mm,  $dRe = 10,000$  and  $\beta u_0 - C_3 / \langle \theta_A \theta_C^2 \rangle$  for three distances from the  $D = 9.4$  mm, and  $Re = 20,000$  and  $D = 4.7$  mm. The correlation release location for  $a Re = 5,000$  and  $D = 4.7$  mm,  $b Re = 10,000$  geometry is shown in Fig 1

$$\chi = \frac{1}{2} \tan^{-1} \left[ \frac{2\vec{\rho}_1 \cdot \vec{\rho}_2}{|\vec{\rho}_2|^2 - |\vec{\rho}_1|^2} \right] \quad (6)$$

and

$$w = 2 \frac{|\vec{\rho}_1 \times \vec{\rho}_2|}{R^2} = 2 \frac{(\rho_{11}\rho_{22} - \rho_{12}\rho_{21})}{R^2} \quad (7)$$

The definitions for  $\chi$  and  $w$  are advantageous because the case with minimum variation with respect to orientation three-point geometric configuration is completely described by these two parameters. In addition,  $\chi$  and  $w$  remain constant as the triangular configuration is translated, rotated, and dilated.

The objective is to evaluate the effects of the size and orientation of the three-point configuration in the inertial-convective regime. The scaling behavior of the three-point correlation functions provides improved understanding of the local structure of the scalar field in comparison to traditional two-point correlation or power spectrum analysis. Two configurations are examined: an isosceles triangle and a collinear arrangement. Figure 11a illustrates the isosceles triangle geometric configuration analyzed in the current study. The shape factor parameters associated with the isosceles geometric configuration are  $\chi = 0.866$  and  $w = 0$ . Similarly, Fig. 11b depicts the collinear geometry. The shape factor parameters for the collinear geometric configuration are  $\chi = 0$  and  $w = \pi/6$ .

These configurations were rotated and dilated to investigate the influence on the orientation angle and the distance between the measurement points. The reported rotation angles correspond to the clockwise direction. When evaluating the exponent, the inertial-convective range was defined as the range between the integral length scale and the case dependent Kolmogorov length scale (Table 1). The exponent was determined via a regression of the correlation function data within the defined length scale range.

The worst case  $R^2$  value of the regression was 0.983 and the value was typically greater than 0.99. The standard error of the exponent estimate was less than 3%.

### 6.2.1 Isosceles configuration

Figure 12 illustrates that the three-point correlation function for the isosceles configuration is approximately equal for each rotation angle. This indicates that the three-point correlation function is nearly independent of the angle between the three-point geometry and the mean scalar gradient for this case. The scaling exponent associated with the global size variable in the inertial-convective regime (Eq. 3) is reported in Fig. 13. Although the scaling exponents are similar in magnitude, there is no suggestion of a universal value.

The dependence of the scaling exponents on the orientation angle and distance from the source provides insights into the local structure of the anisotropic scalar field that traditional two point correlation function or power spectrum analysis does not provide. As shown in Fig. 13a, close to the release location the scaling exponents suggest that the local structure is nearly isotropic for the  $D = 9.4$  mm

case with minimum variation with respect to orientation angle. In contrast, the  $D = 2.2$  mm case shows dependence of the scaling exponent on the orientation angle. In general, the scaling exponent tends to increase in magnitude with increasing intermittency factor. The observed larger magnitude of scaling exponent for the  $D = 2.2$  mm case correlates with the higher intermittency factor shown in Fig. 6. Another important observation in Fig. 13a is that the scaling exponent values for all cases are nearly equal to the local structure of the scalar field in comparison to traditional two-point correlation or power spectrum analysis. However, there exist clear variations between the 0/180 and 90/270 scaling exponents. These variations show that the local structure of the scalar field, while demonstrating symmetry in the horizontal and vertical directions as shown by equivalence in 90/270 and 0/180 cases, is clearly not rotationally invariant.

At intermediate downstream distances ( $2.5/H < 10$ ), a trend emerges that indicates the scaling exponent is roughly independent of the Reynolds number and dependent on the injection length scale. Note that the scaling exponent associated with the different Reynolds numbers are nearly equal, although the exponent for the  $Re = 20,000$  case deviates somewhat from the others. The scaling exponents associated with the different injection length scales are distinctly different: as the injection length scale increases, the magnitude of the scaling exponent decreases due to differences in intermittency.

Farther downstream ( $H > 20$ ), the previously noted trends dissolve. As shown in Fig. 13b, the scaling exponents depend on all parameters. The significant differences between the 0/180 and 90/270 pairs show that the initial horizontal and vertical symmetry (indicated in Fig. 13a) is absent farther downstream. Also, the nozzle diameter case ( $D = 9.4$  mm) that produced relatively isotropic scalar structure near the release location (Fig. 13a), lacks this quality farther downstream (Fig. 13b). This has profound implications as it demonstrates that a turbulent scalar field that is locally isotropic in the inertial convective regime cannot sustain isotropy under the action of turbulent shear dispersion. Another interesting observation is that the variation of the scaling exponent among the nozzle sizes is lower in Fig. 13b compared to in Fig. 13a.

This diminishing dependence on nozzle size shows that the large-scale anisotropy imposed on the small-scale structure

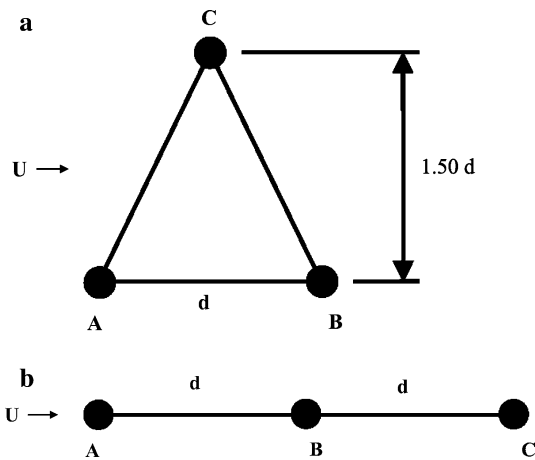


Fig. 11 a The isosceles triangle configuration geometry, and the collinear configuration geometry of the three-point correlation function. The sketched orientations correspond to rotation, and other angles correspond to the clockwise rotation convention

by the varying nozzle size reduces downstream. Furthermore note that the dependence on nozzle size shown in Fig. 13 is non-monotonic, in contrast to that seen in Fig. 6. It is difficult to explain this trend from the current data, but we should note that the non-monotonic dependence with respect to nozzle size is also observed in the intermittent factor plot at  $x/H = 40$  (Fig. 6).

6.2.2 Collinear configuration

For the collinear configuration, the magnitude of the three point correlation function appears sensitive to the rotation angle (Fig. 14). In general, the lowest value of the correlation function is associated with the 45 and the 90 rotation angles. Although there is no clear relationship between the value of the correlation function and the orientation angle, several trends exist. Close to the release location ( $x/H = 1$ , not shown), the largest correlation values are associated with the 0 rotation angle and the lowest correlation values correspond to the 90 rotation angle. This condition is a result of the tracer injection method.

The iso-kinetic release of the tracer preferentially aligns the scalar filaments with the streamwise direction. As a result, the collinear configuration that is aligned with the streamwise direction (i.e. 0) leads to the largest correlation values. As the scalar field evolves downstream, the effects of the injection method diminish, and the behavior of the scalar field is dominated by the mean velocity shear. Therefore, the configuration that aligns with the mean velocity gradient is expected to produce larger correlation values.

Figure 14a confirms the expected results: note that the largest correlation value is associated with the 0 rotation angle, and the smallest correlation values

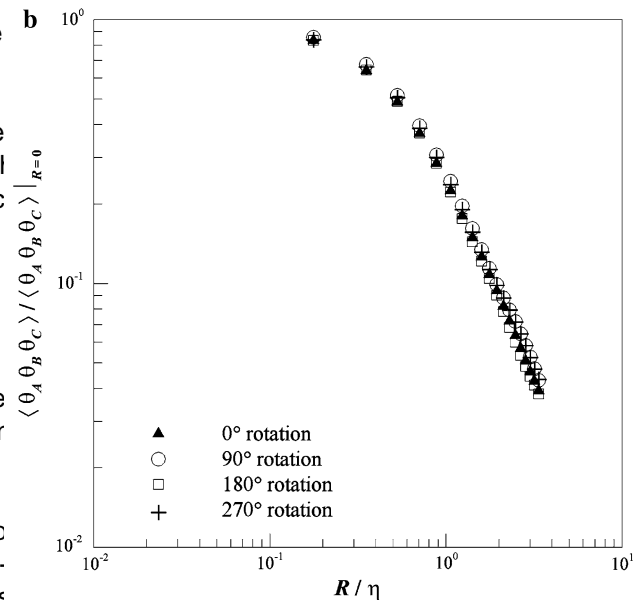
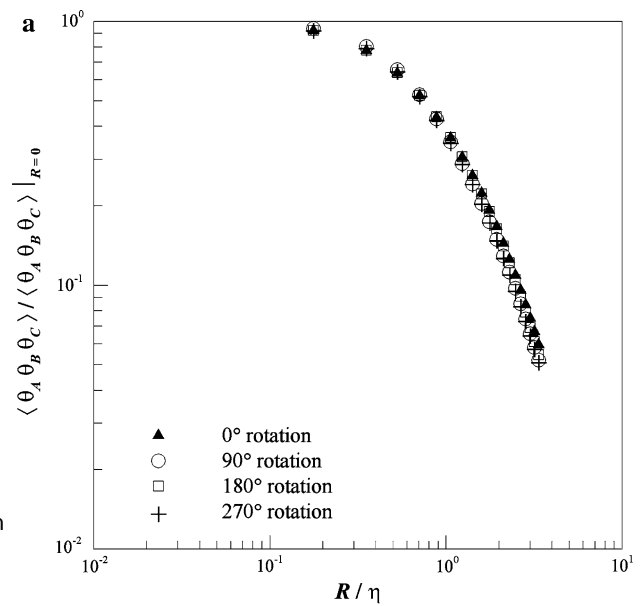


Fig. 12 Three-point correlation function of the fluctuating scalar field for the isosceles configuration for  $Re = 10,000$  and  $D = 4.7$  mm at a  $x/H = 5$ , and b  $x/H = 40$ . The correlation geometry is shown in Fig. 11a

correspond to the +45 rotation angle. The orientation of the collinear configuration that is aligned with the streamwise direction (i.e. 0) leads to the largest correlation values. As a general observation, the effects of the orientation angle of the injection method diminish, and the behavior of the scalar field is dominated by the mean velocity shear corresponding to the highest Reynolds number and the largest injection length scale (i.e. the scalar field is more isotropic).

Additional trends were examined in terms of the scaling exponent for the global size variable (Eq. 3). Although the scaling exponents are similar in magnitude (and similar to

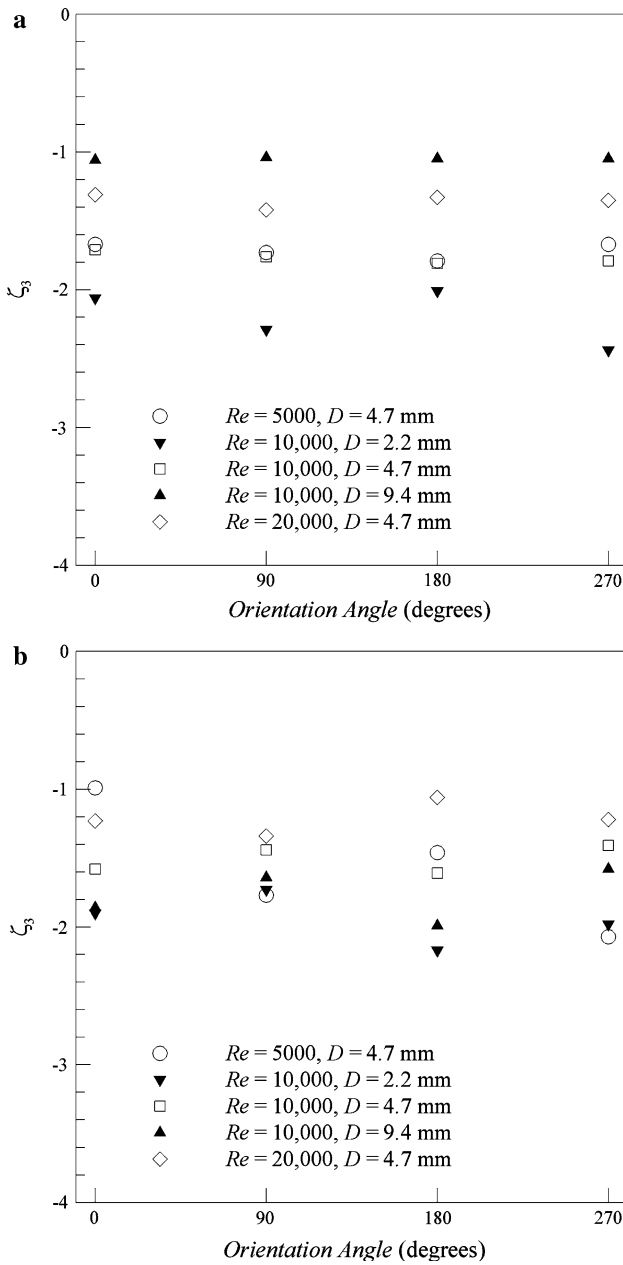


Fig. 13 The scaling exponent in the inertial-convective regime of the three-point correlation function for the isosceles configuration at a  $x/H = 5$ , and b  $x/H = 40$

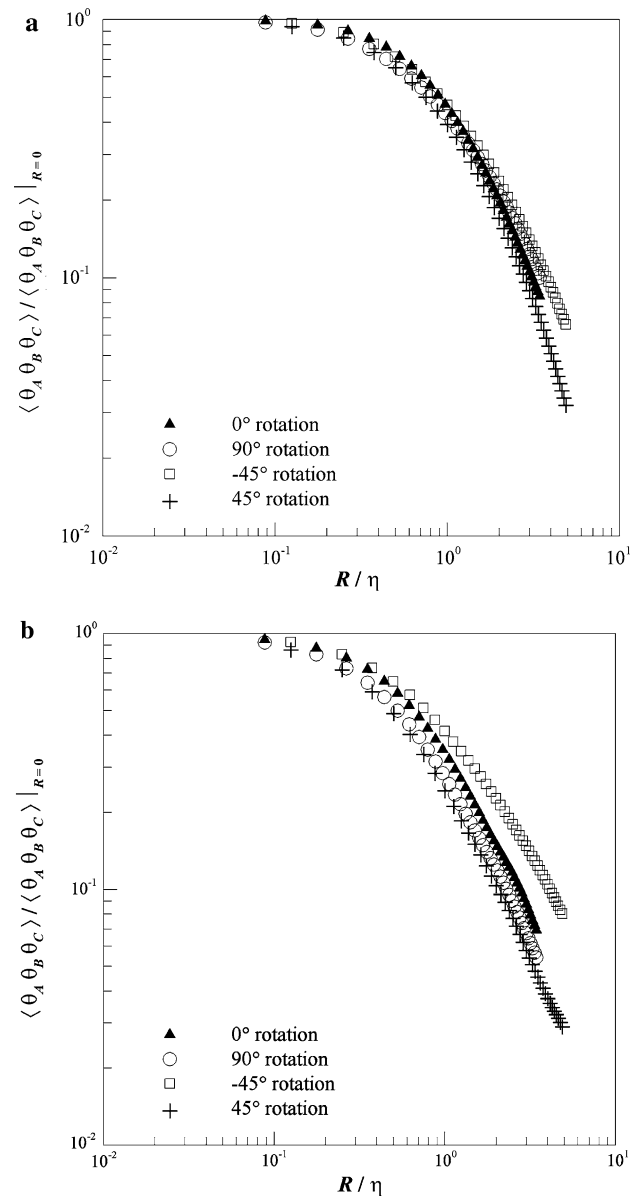


Fig. 14 Three-point correlation function of the fluctuating scalar field for the collinear configuration for  $Re = 10,000$  and  $D = 4.7$  mm at a  $x/H = 5$ , and b  $x/H = 40$ . The correlation geometry is shown in Fig. 11b

that observed in Fig. 13, there is no discernable convergence with the theoretical predictions by Falkovich et al. (2001), to a universal value (Fig. 15). At intermediate downstream distances ( $2.5 < x/H < 10$ ), the data suggests that the scaling exponent is roughly independent of the Reynolds number and dependent on the injection length. Figure 15a illustrates that as the injection length scale increases, the magnitude of the scaling exponent decreases. This trend was also observed for the isosceles geometric configuration. The trend with injection length scale is less apparent farther downstream, i.e.  $x/H > 20$  (Fig. 15b). The current results agree fairly well with the current study evaluated multipoint correlation functions for a passive scalar field in a turbulent shear flow. The

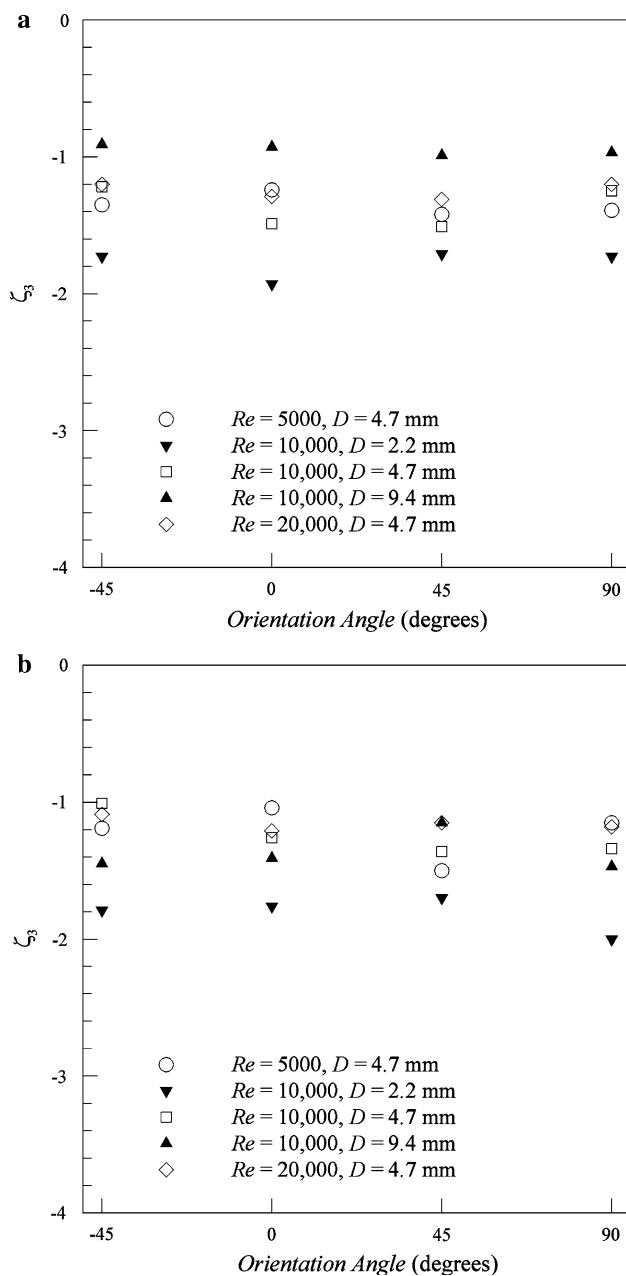


Fig. 15 The scaling exponent in the inertial-convective regime of the three-point correlation function for the collinear configuration at a  $x/H = 5$ , and b  $x/H = 40$

field corresponds to the plume downstream of an elevated release location in a fully developed open channel turbulent boundary layer. Statistical averages were calculated by ensemble-averaging over the period of the record and also by spatially averaging over a region of the field in which the mean concentration gradient was constant. Two-point correlations of the fluctuating scalar field were calculated in the streamwise and wall-normal directions to estimate the integral length scale in each direction. The two-point correlation contours exhibit a tilted, asymmetric elliptical

shape that develops as a result of the mean velocity shear. Therefore, the current study agrees with the experimental results presented by Tavoularis and Corrsi (1981) and illustrates the inherent anisotropic behavior of the scalar field.

The results of the Mydlarski and Warhaft (1998) configuration indicate that the contours of the three-point correlation function were indeed symmetric in the modified coordinate system as previously reported for nearly homogeneous and isotropic turbulent flow. The symmetry associated with well-correlated points was represented by concentric, circular contours, which suggested universal behavior of the fluctuating scalar field for well-correlated points. The outermost contours maintain symmetric properties but evolved into a concave-sided hexagonal shape that resembled the V-shape reported by Mydlarski and Warhaft (1998). The effects of mean velocity shear and scalar (signal) skewness may explain the less distinct V-shape contour pattern that was observed for lower Reynolds number and smaller nozzle diameter.

The current study also examined isosceles and collinear three-point configurations. The effects of the size and orientation of the three-point template were evaluated because the shape factor remains constant for a specified geometric configuration. In the inertial-convective regime, the orientation angle affected the value of the correlation function for the both isosceles and collinear configurations indicating a fundamentally anisotropic field. The scaling exponent appeared to be roughly independent of the Reynolds number and dependent on the injection length scale at intermediate downstream distances ( $2.5/H < 10$ ). The scaling exponent varied between 0.9 and  $-2$  regardless of the three-point geometry.

**Acknowledgments** The authors gratefully acknowledge the financial support provided by the National Science Foundation (CTS-0303406).

## References

- Celani A, Vergassola M (2001) Statistical geometry in scalar turbulence. *Phys Rev Lett* 86:424–427
- Celani A, Lanotte A, Mazzino A, Vergassola M (2000) Universality and saturation of intermittency in passive scalar turbulence. *Phys Rev Lett* 84:2385–2388
- Chatwin PC, Sullivan PJ (1989) The intermittency factor of scalars in turbulence. *Phys Fluids A* 1:761–763
- Dasi LP (2004) The small-scale structure of passive scalar mixing in turbulent boundary layers. PhD thesis, Georgia Institute of Technology, Atlanta, Georgia
- Dasi LP, Schuerg F, Webster DR (2007) The geometric properties of high Schmidt number passive scalar iso-surfaces in turbulent boundary layers. *J Fluid Mech* 588:253–277
- Falkovich G, Gawedzki K, Vergassola M (2001) Particles and fields in fluid turbulence. *Rev Mod Phys* 73:913–975

- Ferrier AJ, Funk DR, Roberts PJW (1993) Application of optical techniques to the study of plumes in stratified fluids. *Dyn Atmos Oceans* 20:155–183
- Holzer M, Siggia ED (1994) Turbulent mixing of a passive scalar. *Phys Fluids* 6:1820–1837
- Mestayer PG, Gibson CH, Coantic MF, Patel AS (1976) Local anisotropy in heated and cooled turbulent boundary layers. *Phys Fluids* 19:1279–1287
- Mydlarski L, Warhaft Z (1998) Three-point statistics and the anisotropy of a turbulent passive scalar. *Phys Fluids* 10:2885–2894
- Mydlarski L, Pumir A, Shraiman BI, Siggia ED, Warhaft Z (1998) Structures and multipoint correlators for turbulent advection: predictions and experiments. *Phys Rev Lett* 81:4373–4376
- Pumir A (1994) A numerical study of the mixing of a passive scalar in three dimensions in the presence of a mean gradient. *Phys Fluids* 6:2118–2132
- Pumir A (1998) Structure of the three-point correlation function of a passive scalar in the presence of a mean gradient. *Phys Rev E* 57:2914–2929
- Schumacher J, Sreenivasan KR (2003) Geometric features of the mixing of passive scalars at high Schmidt numbers. *Phys Rev Lett* 91: 174501–174501-4
- Shraiman BI, Siggia ED (1995) Anomalous scaling of a passive scalar in turbulent flow. *Comptes rendus de l'Académie des sciences Series IIb* 321:279–284
- Shraiman BI, Siggia ED (1996) Symmetry and scaling of turbulent mixing. *Phys Rev Lett* 77:2463–2466
- Shraiman BI, Siggia ED (1998) Anomalous scaling for a passive scalar near the Batchelor limit. *Phys Rev E* 57:2965–2977
- Shraiman BI, Siggia ED (2000) Scalar turbulence. *Nature* 405:639–646
- Spalart PR (1988) Direct simulation of a turbulent boundary-layer up to  $Re_\theta = 1410$ . *J Fluid Mech* 187:61–98
- Sreenivasan KR, Antonia RA, Britz D (1979) Local isotropy and large structures in a heated turbulent jet. *J Fluid Mech* 94:745–775
- Tachie MF, Balachandar R, Bergstrom DJ (2003) Low Reynolds number effects in open-channel turbulent boundary layers. *Exp Fluids* 34:616–624
- Tavoularis S, Corrsin S (1981) Experiments in nearly homogeneous turbulent shear flow with a uniform mean temperature gradient. Part 1. *J Fluid Mech* 104:311–347
- Tong C, Warhaft Z (1994) On passive scalar derivative statistics in grid turbulence. *Phys Fluids* 6:2165–2176
- Warhaft Z (2000) Passive scalars in turbulent flows. *Annu Rev Fluid Mech* 32:203–240